and C. E. Max. This work was performed under the auspices of the U. S. Department of Energy, at the Lawrence Livermore Laboratory under Contract No. W-7405-Eng-48.

---

[1] V. P. Silin, Zh. Eksp. Teor. Fiz. 47, 2254 (1964) [Sov. Phys. JETP 20, 1510 (1965)].

[2] R. E. Kidder, in *Physics of High Energy Density*, edited by P. Caldirola and H. Knoepfel (Academic, New York, 1971), p. 306.

[3] P. J. Catto and T. Speziale, Phys. Fluids 20, 167 (1977).

[4] For recent results and listings of earlier work see Y. Shima and H. Yatom, Phys. Rev. A 12, 2106 (1975); H. Brysk, J. Phys. A 8, 1260 (1975); L. Schlessinger and J. Wright, Phys. Rev. A 20, 1934 (1979).

[5] J. Dawson and C. Oberman, Phys. Fluids 5, 517 (1962); T. W. Johnston and J. M. Dawson, Phys. Fluids 16, 722 (1973).

[6] S. I. Braginskii, in *Reviews of Plasma Physics*, edited by M. A. Leontovich (Consultants Bureau, New York, 1965), Vol. 1, p. 205.

[7] I. P. Shkarofsky, T. W. Johnston, and M. P. Bachynski, *The Particle Kinetics of Plasmas* (Addison-Wesley, Reading, Mass. 1966).

[8] H. D. Shay, R. A. Haas, and W. L. Kruer *et al.*, Phys. Fluids 21, 1634 (1978).

[9] B. A. Trubnikov, in *Reviews of Plasma Physics*, edited by M. A. Leontovich (Consultants Bureau, New York, 1965), Vol. 1, p. 174.

[10] J. Killeen, A. A. Mirin, and M. E. Rensink, in *Methods in Computational Physics*, edited by J. Killeen (Academic, New York, 1976), Vol. 16, p. 389.

[11] The same velocity dependence arises in electron heating by ion waves with an isotropic spectrum, as shown in the two-dimensional case by R. Z. Sagdeev and A. A. Galeev, in *Nonlinear Plasma Theory* (Benjamin, New York, 1969), Chap. 2.

[12] On the other hand, electrons quickly cross the intensity modulations in a standing wave, so that one should then use simply the spatial average of v_0^2.

[13] J. Dawson and C. Oberman, Phys. Fluids 6, 394 (1963).

Spatially Resolved Suprathermal X-Ray Emission from Laser-Fusion Targets

N. M. Ceglio and J. T. Larsen
Lawrence Livermore Laboratory, University of California, Livermore, California 94550
(Received 29 October 1979)

High-resolution images of suprathermal x-ray emission from laser-imploded fusion targets have been recorded. The images show the spatial distribution of the relatively cold pusher material during the early stages of target implosion. There is evidence of an early, asymmetric breakup of the pusher shell.

X-ray emission spectra from laser-driven fusion targets commonly exhibit a suprathermal x-ray (STX) component.[1] The STX's are bremsstrahlung produced by radiative interactions between suprathermal electrons (STE's) and background plasma ions, and as such are characteristic of a significant STE population. The physical mechanisms governing the production and transport of STE's are vital to an understanding of laser-driven implosions. Images of the STX emission can provide insight into these mechanisms.

This Letter reports the first high-resolution images of the suprathermal x-ray emission from laser-driven fusion targets. The images (1) show the distribution of the relatively cold pusher material during target irradiation, (2) provide evidence of breakup of the pusher during the early stages of implosion, and (3) illustrate spatial inhomogeneities in suprathermal electron production.

The STX imaging experiments were conducted using the Shiva laser-target irradiation facility at Lawrence Livermore Laboratory. This laser system produces a twenty-beam, multiterawatt pulse of 1.06-μm radiation. Typical pulse duration for these experiments was 90 psec, with 17–20 TW delivered to the target. The twenty beams were focused onto the target in two opposing ten-beam clusters. The typical target was a spherical glass microshell (o.d. ~ 300–325 μm; wall thickness ~ 1.5–2.0 μm) with an equimolar DT gas fill ~ 2 mg/cm^3. Typical target yield was $(0.5-1.0)\times 10^{10}$ neutrons.

High-resolution, time-integrated images of the STX emission from these exploding pusher targets were obtained using a coded imaging technique, zone-plate coded imaging.[2,3] The zone-plate camera subtended a solid angle $\sim 4\times 10^{-2}$ sr, had a 3-cm target–to–zone-plate distance, and had a nominal resolution of 20 μm. The coded aperture was a gold Fresnel zone plate of 240 zones, 24 μm thick, with a minimum zone width of 10 μm. Coded x-ray images were recorded in a multilayer film pack comprised of several film layers separated by various low-Z filter foils.[4] This arrangement allowed us to record simultaneously, on a single shot with a single camera, a series of x-ray images in separated energy channels.

Image data[5] representative of this target-shot series are presented in Figs. 1 and 2. Figure 1(a) is an image of the thermal x-ray (TX) and Fig. 2 an image of the STX emission typical for the target-shot series under discussion.

There are distinctive differences between the TX and STX images. The TX image is dominated by emission from two disk-shaped regions of hot, stagnated pusher material near the target center. The emission exhibits a distinct minimum at target center—the locus of the compressed, low-Z fuel. The STX image, on the other hand, is dominated by a thin symmetrical shell of emission emanating from the region of the unimploded pusher, although there are small "thermal" contributions from the hot, stagnated pusher material near target center.

A LASNEX simulation[6] for a set of representative parameters characteristic of this class of short-pulse exploding-pusher experiments has been run. The code generated time-integrated images of the TX and STX emission in the spectral windows matching those of the zone-plate camera. The simulated TX and STX images are presented in Figs. 1(b) and 3, respectively. Note the good qualitative agreement between the measured and calculated images [compare Figs. 1(a) and 1(b) for TX images; compare Figs. 2 and 3

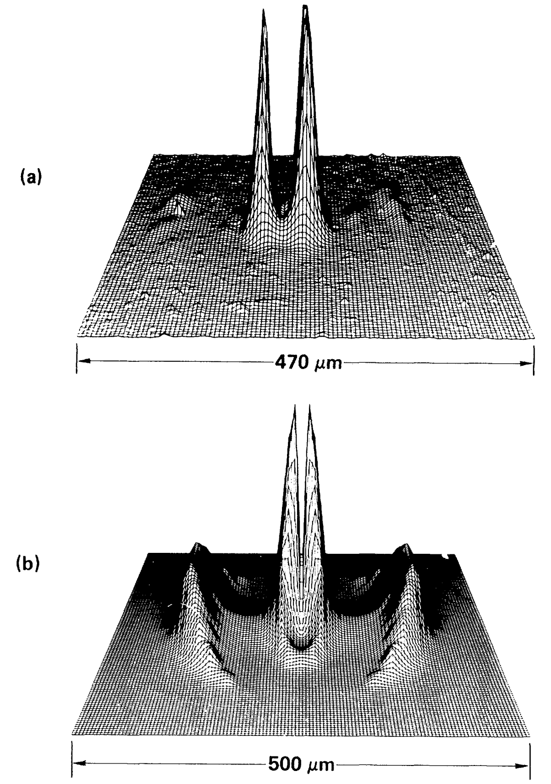

FIG. 1. (a) Measured and (b) calculated thermal x-ray images in the spectral window 4–7 keV (full width at half maximum). Image intensity is plotted vertically vs the two spatial dimensions. The images are dominated by emission from two disk-shaped regions of hot, stagnated (separated by the compressed, low-Z fuel) pusher material near target center. In the calculation (b) an effective inhibition factor $\simeq 0.03$ was used for the thermal electron transport.

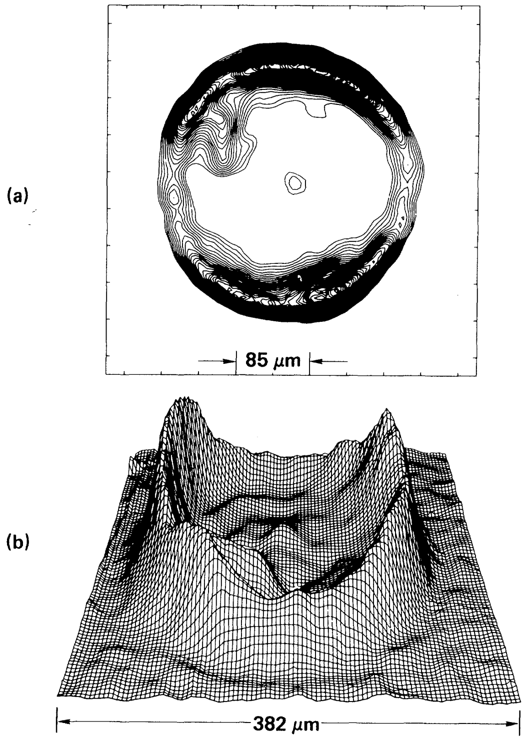

FIG. 2. Suprathermal x-ray image in the spectral window 17–30 keV (full width at half maximum). Laser power was 19.9 TW; target o.d. = 298 μm with 1.5-μm wall; neutron yield = 1×10^{10}. (a) A 2D isointensity contour map of emission intensity; (b) a 3D representation of the image data (see Ref. 5). The dominant image feature is the hollow shell structure of diameter roughly equal that of the original microballoon.

for STX images].

Detailed interpretation of the STX images is facilitated by studying the expression for the image intensity,

$$I(x,y) = \int dz \int d\epsilon \int dt\, N_e(x,y,z,\epsilon,t) \times N_i(x,y,z,t) v\sigma(\epsilon). \quad (1)$$

In the above $I(x,y)$ is the time-integrated, two-dimensional distribution of the STX emission in the spectral window of the zone-plate camera; N_e is the STE density; N_i is the pusher ion density ($\bar{Z} \simeq 10$); σ is the bremsstrahlung cross section for a STE at energy ϵ emitting into the spectral window of interest; and v is the STE speed. The STE's contributing to the STX images are presumably produced near the critical density surface during the time of intense laser irradiation of the target, have a slowing-down time (to $\epsilon < 17$ keV) on the order of 10 psec, have a collision mean free path much greater than the target diameter, and have a target-traversal time on the order of a few picoseconds.

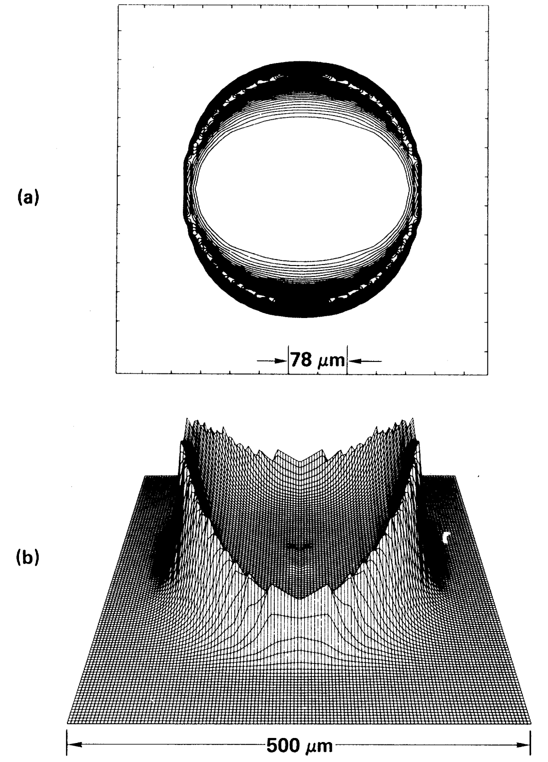

FIG. 3. Computer simulation of the STX emission in the 17–30-keV spectral band for a set of parameters representative of the class of exploding-pusher experiments under investigation: Laser power = 18.5 TW; target o.d. = 322 μm with 2-μm wall; neutron yield = 9 $\times 10^9$. These conditions are the same as those used for the calculated TX image of Fig. 1(b). There is good qualitative agreement between the above images and those of Fig. 2. The absence of a weak thermal contribution (at target center) to the image in (a) is merely due to our particular choice of contour levels and intervals. A close inspection of (b) does show a weak contribution from the hot stagnated pusher material near target center.

The STX image is, therefore, a weighted product of the STE density (N_e) and ion pusher density (N_i), integrated along the camera line of sight ($\int dz$) and integrated over the time of STE production—a short time (less than the full width at half maximum of the laser pulse) around the peak of the laser irradiation. In the case of a relatively uniform STE spatial distribution, the STX image would simply be a mapping of the pusher ion distribution around the time of intense laser irradiation, i.e., the early stages of target implosion.[7] This accounts for the general "hollow shell" structure of the calculated and measured STX images but cannot account for other image details discussed in the following paragraphs.

Superimposed on the hollow shell structure of the STX images are a number of interesting features: (α) slow azimuthal variation of emission intensity around the pusher shell reducing to a minimum in the equatorial plane of the target (Figs. 2 and 3); (β) small-scale, rapid fluctuations (or bumps) in emission intensity around the pusher shell—superimposed on the slow variation noted in (α) (Fig. 2); (γ) a protuberance on the interior pusher shell surface (Fig. 2). Feature (α) can be attributed to the variation of incident laser intensity—which produces variation in STE production and N_e—over the target surface. The laser intensity at the target surface is a minimum in the equatorial plane normal to the directions of the two opposing ten-beam clusters, thus accounting for the image intensity minimum in that region.

Feature (α) is apparent in both measured and calculated STX images. Features (β) and (γ) are interesting in that they appear only in the measured image, thereby representing departures from the simulations. The localized fluctuations of feature (β) are most likely indicative of nearby regions of preferred STE production caused by small-scale hot spots and nonuniformities in the incident laser irradiation pattern on target. The protuberance noted as feature (γ), since it occurs on the pusher-shell interior, is most likely a nonuniformity in pusher-ion density (N_i) indicative of breakup of the pusher shell during target irradiation.

In addition to the above observations, the STX images provide some information about STE transport in short-pulse, exploding-pusher, microsphere targets. The STX simulation of Fig. 3 includes neither STE transport inhibition[8] nor enhanced azimuthal transport of STE's in the target sheath.[9] The good agreement between the images of Figs. 2 and 3 indicate that under favorable experimental conditions (i.e., quasiuniform illumination—no hot spots) such STE transport mechanisms probably do not play an important role in this class of laser fusion experiments.

We wish to acknowledge the assistance of our Lawrence Livermore Laboratory colleagues H. G. Ahlstrom, D. T. Attwood, Y. L. Pan, G. Howe, D. Ciarlo, C. Dittmore, W. Herrman, G. Stone, and the Shiva laser crew. This work was performed under the auspices of the U. S. Department of Energy under Contract No. W-7405-ENG-48.

---

[1] J. F. Kephart, R. P. Godwin, and G. H. McCall, Appl. Phys. Lett. 25, 108 (1974); V. W. Slivinsky, H. N. Kornblum, and H. D. Shay, J. Appl. Phys. 46, 1973 (1975); B. H. Ripin, *et al.*, Phys. Rev. Lett. 34, 1313 (1975).

[2] High-resolution imaging of the STX emission was found to be beyond the capabilities of pinhole and grazing incidence reflection techniques because of the low flux levels and high energies involved.

[3] Zone-plate coded imaging is a two-step imaging technique. In the first step the x-ray source casts a shadowgraph through a Fresnel zone plate onto an appropriate film. Image reconstruction (step two) is achieved optically with methods similar to holographic reconstruction. For further details see N. M. Ceglio, *et al.*, J. Appl. Phys. 48, 1563 (1977), and 48, 1566 (1977), and Phys. Rev. Lett. 39, 20 (1977).

[4] A layer in this pack consists of a filter foil followed by three single-sided x-ray films—types *M*, *R*, and *FGP*. The foil material, thickness, and x-ray image energies for the various layers are as follows: layer 1, Be, 150 μm, 4–7 keV; layer 2, Al, 250 μm, 10–20 keV; layer 3, Al, 1250 μm, 17– 30 keV.

[5] The image data format for all the figures is as follows: In the two-dimensional (2D) contour maps each contour is a locus of constant x-ray emission intensity. The incremental intensity change is constant between successive contours. In the 2D plots the two opposing ten-laser beam clusters are incident on the target from top and bottom. In the 3D plots the beam clusters are incident from the left and right, respectively. "Left" on the 3D plots corresponds to "top" on the 2D plots.

[6] LASNEX is a 2D Lagrangian, magnetohydrodynamics code with multigroup electron transport. For further details see G. B. Zimmerman, Lawrence Livermore Laboratory Report No. UCRL-78411, 1973 (unpublished).

[7] In these short-pulse, large-ball experiments, peak target compressions occur well after the peak of the laser pulse.

[8] S. Braginskii, *Reviews of Plasma Physics* (Consultants Bureau, New York, 1965), Vol. 1, p. 205.

[9] J. R. Albritton *et al.*, Phys. Rev. Lett. 39, 1536 (1977).

Structural Stability of 495 Binary Compounds

Alex Zunger
Solar Energy Research Institute, Golden, Colorado 80401

(Received 18 June 1979)

With use of the characteristic turning-point radii of the first-principles nonlocal density-functional atomic pseudopotentials, a successful topological prediction of the crystal structures of 495 binary *AB* compounds of transition and simple elements is obtained.

There are about 500 stable, near-stoichiometric, ordered binary solids made of atoms belonging to the first five rows of the periodic table whose crystal structure has been determined experimentally. Most of these crystals appear in their most stable form in one of about twenty distinct spatial structures. In this Letter I show that a simple nonempirical quantum mechanical approach, based on the density-functional nonlocal pseudopotential concept, explains this distribution diagrammatically with striking success.

Even before the pioneering studies of Goldschmidt, Pauling, and others[1] it was known ther-